Abrupt shape transition at neutron number $N = 60$: $B(E2)$ values in ^{94,96,98}Sr from fast γ-γ timing

J.-M. Régis,[1,*] J. Jolie,[1] N. Saed-Samii,[1] N. Warr,[1] M. Pfeiffer,[1] A. Blanc,[2] M. Jentschel,[2] U. Köster,[2] P. Mutti,[2] T. Soldner,[2] G. S. Simpson,[3,†] F. Drouet,[3] A. Vancraeyenest,[3] G. de France,[4] E. Clément,[4] O. Stezowski,[5] C. A. Ur,[6] W. Urban,[7] P. H. Regan,[8,‡] Zs. Podolyák,[8] C. Larijani,[8,§] C. Townsley,[8] R. Carroll,[8] E. Wilson,[8] L. M. Fraile,[9] H. Mach,[9,‖] V. Paziy,[9] B. Olaizola,[9] V. Vedia,[9] A. M. Bruce,[10] O. J. Roberts,[10] J. F. Smith,[11] M. Scheck,[11] T. Kröll,[12] A.-L. Hartig,[12] A. Ignatov,[12] S. Ilieva,[12] S. Lalkovski,[13,‖] W. Korten,[14] N. Mărginean,[15] T. Otsuka,[16,¶] N. Shimizu,[16] T. Togashi,[16] and Y. Tsunoda[16]

[1]*Institut für Kernphysik der Universität zu Köln, Zülpicher Str. 77, 50937 Köln, Germany*
[2]*Institut Laue-Langevin, 71 avenue des Martyrs, 38042 Grenoble Cedex, France*
[3]*LPSC, 53 avenue des Martyrs, 38026 Grenoble Cedex, France*
[4]*Grand Accélérateur National d'Ions Lourds (GANIL), CEA/CRF-CNRS/IN2P3, 14076 Caen Cedex 05, France*
[5]*IPN de Lyon, 4, Rue Enrico Fermi, 69622 Villeurbanne Cedex, France*
[6]*INFN, via Marzolo 8, 35131 Padova, Italy*
[7]*Faculty of Physics, University of Warsaw, ul. Hoza 69, PL-00-681 Warsaw, Poland*
[8]*Department of Physics, University of Surrey, Guildford GU2 7XH, United Kingdom*
[9]*Grupo de Fisica Nuclear, FAMN, Universidad Complutense, 28040 Madrid, Spain*
[10]*SCEM, University of Brighton, Lewes Road, Brighton BN2 4GJ, United Kingdom*
[11]*School of Engineering, University of the West of Scotland, Paisley PA1 2BE, United Kingdom*
[12]*Institut für Kernphysik, TU Darmstadt, Schlossgartenstr. 9, 64289 Darmstadt, Germany*
[13]*Faculty of Physics, University of Sofia, 1164 Sofia, Bulgaria*
[14]*CEA, IRFU, Université Paris-Saclay, 91191 Gif-sur-Yvette, France*
[15]*Horia Hulubei NIPNE, 77125 Bucharest, Romania*
[16]*Center for Nuclear Study, University of Tokyo, Hongo, Bunkyo-ku, Tokyo 113-0033, Japan*
(Received 21 February 2017; published 23 May 2017)

Lifetimes of low-lying yrast states in neutron-rich ^{94,96,98}Sr have been measured by Germanium-gated γ-γ fast timing with LaBr3(Ce) detectors using the EXILL&FATIMA spectrometer at the Institut Laue-Langevin. Sr fission products were generated using cold-neutron-induced fission of ^{235}U and stopped almost instantaneously within the thick target. The experimental $B(E2)$ values are compared with results of Monte Carlo shell-model calculations made without truncation on the occupation numbers of the orbits spanned by eight proton and eight neutron orbits and show good agreement. Similarly to the Zr isotopes, the abrupt shape transition in the Sr isotopes near neutron number $N = 60$ is identified as being caused by many-proton excitations to its $g_{9/2}$ orbit.

I. INTRODUCTION

It is well known that the ground states of the Sr isotopes with proton number $Z = 38$ and the Zr isotopes ($Z = 40$) show an abrupt change from a spherical structure at neutron number $N = 58$ to a strongly deformed structure at $N = 60$. In a spherical shell-model approach, this phenomenon was first explained by the fact that once the neutron $\nu g_{7/2}$ orbit is being filled, the proton subshell suddenly disappears due to the $\nu g_{7/2}$-$\pi g_{9/2}$ interaction [1]. In a Nilsson approach, the phenomenon was explained by strongly interacting proton and neutron Nilsson orbits ([2] and references therein). For the neutrons, the down-sloping $\nu 1/2^-[550]$ and the $\nu 3/2^-[541]$ intruder orbits, both resulting from the spherical $h_{11/2}$ orbit, drive the deformation. Meanwhile, the extruder $\nu 9/2^+[404]$ orbit stabilizes the deformation parameter at a saturation level of about $\beta = 0.4$. On the other hand, for the protons, the down-sloping $\pi 1/2^+[440]$ and the $\pi 3/2^+[431]$ orbits, originating from the spherical $g_{9/2}$ orbit, are fully occupied at $Z = 38$ and $Z = 40$, again at a deformation parameter of about 0.4. These proton intruder orbits have a large spatial overlap with the neutron intruder orbits, creating a minimum in the binding energy at $\beta = 0.4$. At $N = 60$, the effective single-particle energy of the deformed configuration is lower than that of the spherical one and the deformed configuration becomes the ground state. Thus, the sudden onset of the deformation can be explained at least qualitatively in connection to the proton $g_{9/2}$ orbit.

In principle, a shell-model calculation can reproduce shape transitions, however, its application encounters some limits in the size of the calculation (the largest dimension reaches 3.7×10^{23} for the Zr isotopes). Recently, a large-scale Monte

*regis@ikp.uni-koeln.de
†Present address: School of Engineering, University of the West of Scotland, Paisley PA1 2BE, United Kingdom.
‡Present address: National Physical Laboratory, Teddington, Middlesex TW11 0LW, United Kingdom.
§Present address: National Centre for Nuclear Research, ul. Hoza 69, Warsaw, Poland.
‖Present address: Department of Physics, University of Surrey, Guildford GU2 7XH, United Kingdom.
¶Present address: Department of Physics, University of Tokyo, Hongo, Bunkyo-ku, Tokyo 113-0033, Japan: NSCL, Michigan State University, East Lansing, Michigan 48824, USA; Instituut voor Kern- en Stralingsfysica, KU Leuven, B-3001 Leuven, Belgium.

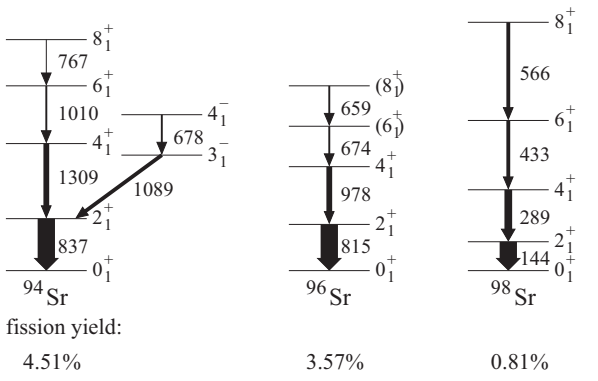

FIG. 1. γ-ray transitions in Sr isotopes as observed after neutron-induced fission of ^{235}U using the EXILL&FATIMA spectrometer, which was installed at a cold-neutron guide of the ILL reactor. The relative γ-ray intensities are indicated by the widths of the transition arrows. The isotopic yields for thermal-neutron-induced fission of ^{235}U are taken from Ref. [13].

Carlo shell-model (MCSM) calculation has been carried out for Zr isotopes in the $N = 50$–70 region without truncation of the model space [3]. Level energy and $B(E2)$ values were obtained within a single framework in good agreement with experiments, depicting the abrupt shape transition at $N = 60$ as a consequence of type II shell evolution involving many proton particle-hole excitations to the $g_{9/2}$ orbit [3,4]. Let us briefly explain the type II shell evolution. We start with the usual (type I) shell evolution, where some single-particle orbits (for example the proton $1f_{7/2}$-$1f_{5/2}$ splitting) change their energies due to the occupancy of other particular orbits (neutron $1g_{9/2}$ orbit, in the present example). This happens when more neutrons or protons are added (neutrons in $1g_{9/2}$, in the present example) and implies an evolution in shape across different nuclei as a function of N or Z. The driving forces to this change are tensor and central forces. Type II shell evolution is due to the same kind of nuclear forces, but the occupancies are changed not by the addition of neutrons (or protons) but by particle-hole excitations within the same nucleus. In the above example, the neutron $1g_{9/2}$ orbits can contain more neutrons by creating holes in the pf shell. By choosing optimum orbits for holes, similar effects can occur in the proton orbits (further reduction of the proton $1f_{7/2}$-$1f_{5/2}$ splitting due to holes in the neutron $1f_{5/2}$ orbit, in the present example). Such changes of single-particle energies can enhance the deformation in appropriate cases if rather many particle-hole excitations occur. Thus, type II shell evolution is often connected to the sudden onset of large deformation or the coexistence of different shapes. Detailed explanation on the type II shell evolution are given in Ref. [4], particularly with Fig. 1, while discussions with concrete cases can be found in Ref. [3] for Zr isotopes and in Ref. [5] for Ni isotopes.

We have performed fast-timing experiments on ^{94,96,98}Sr isotopes using the $LaBr_3$(Ce) detectors of the FATIMA Collaboration and part of the EXOGAM array at the PF1B neutron guide of the Insitut Laue-Langevin (ILL) in Grenoble, France. The advantage here is that prompt γ rays of neutron-induced secondary fission fragments are measured, allowing us to access information on excited states of about 100 exotic nuclei within a single experiment. γ rays feeding and decaying from excited states have been used for direct electronic lifetime measurements of these states. Highly precise lifetime results have been obtained using this EXILL&FATIMA spectrometer by means of centroid (i.e., the center of gravity of a γ-γ time distribution) measurements [6–11]. Partial level schemes of neutron-rich Sr isotopes with γ rays as observed using the EXILL&FATIMA spectrometer are shown in Fig. 1. We would like to present MCSM calculations on these even-even Sr isotopes with a focus on the shape transition at $N = 60$ (^{98}Sr) and compare the results with experimental values derived in this work. The results are also compared with other theoretical models based on the density functional theory [12].

II. EXPERIMENTAL SETUP, METHODS, AND RESULTS

To access nuclear excited states of neutron-rich fission fragments, prompt-fission γ-ray spectroscopy experiments using a mixed array consisting of eight EXOGAM Clover-Ge and 16 $LaBr_3$(Ce) detectors have been performed at the ILL within the EXILL&FATIMA campaign. The mixed array was installed at the exit of the collimation line of the cold-neutron guide PF1B [14,15] of the ILL reactor. The collimated cold-neutron beam 12 mm in diameter provided a flux of 10^8 neutrons per second and cm^2 at the target position to induce fission in ^{235}U. 0.675 mg UO_2 was sandwiched between two 25-μm thick Be backings, in order to stop the fission fragments within the target in a few ps. While the good energy resolution of the Ge detectors allows for precise selection of a triple γ-γ-γ cascade, the excellent timing performance of the $LaBr_3$ detectors is used for time-difference measurements between the γ rays feeding and decaying from an excited state in the 10 ps to 10 ns region using analog time-to-amplitude converters (TACs). Time-stamped data has been acquired and sorted off line to provide Ge-$LaBr_3$-Ge events for coincidence analysis and Ge-$LaBr_3$-$LaBr_3$-TAC events for lifetime determination. More information on the digital data acquisition system, the fast-timing electronics setup and the sorting procedures can be found in Ref. [16].

In a first step of the analysis, the Ge-$LaBr_3$-Ge events are used to investigate for good Ge and $LaBr_3$ gates, i.e., narrow energy windows set on full-energy peaks (FEPs), which allow us to unambiguously disentangle the cascade of the nucleus of interest out of the rather complex prompt-fission γ-ray spectrum. Most importantly, the Ge plus $LaBr_3$ doubly gated $LaBr_3$ coincidence spectrum should be clean, meaning that no other γ rays contribute to the second FEP of the γ-γ cascade to be measured with the $LaBr_3$ detectors for lifetime determination. Such a coincidence analysis is illustrated in Fig. 2 for the case of the 2_1^+ state in ^{96}Sr. The Ge coincidence spectrum with Ge gate on the $6_1^+ \rightarrow 4_1^+$ 674-keV transition presented in Fig. 2(a) shows strong transitions in the cascade belonging to ^{96}Sr and also many other transitions, which may belong to other nuclei. However, the FEP of the $4_1^+ \rightarrow 2_1^+$ transition at 978 keV is clean and is also clearly seen in the Ge-gated $LaBr_3$ coincidence spectrum as a single peak. The advantage of using a clean $LaBr_3$ gate is depicted in Fig. 2(b). The Ge(674)-$LaBr_3$(978) doubly gated Ge coincidence

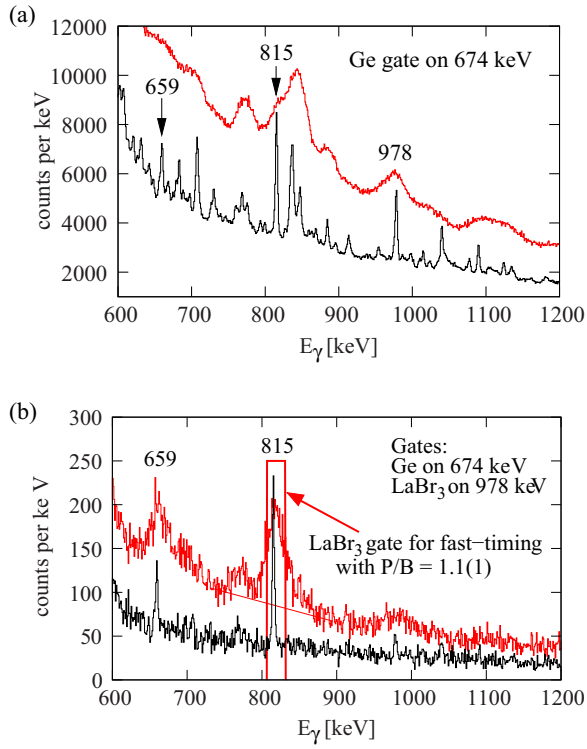

FIG. 2. (a) Ge-gated coincidence spectra out of triple Ge-$LaBr_3$-Ge events showing transitions in ^{96}Sr. The $LaBr_3$ coincidence spectrum is plotted in red. Part of the ^{96}Sr level scheme is shown in Fig. 1. (b) Ge plus $LaBr_3$ doubly gated coincidence spectra. The $LaBr_3$ coincidence spectrum is generated using Ge-$LaBr_3$-$LaBr_3$-TAC events (projection of $LaBr_3$-TAC matrix). The coincidence time window is 120 ns.

spectrum is dramatically improved; the FEP of the $2_1^+ \rightarrow 0_1^+$ 815-keV transition dominates and no other γ ray, which could contaminate the FEP in the $LaBr_3$ coincidence spectrum and falsify the lifetime determination, is close to it.

The second step of the analysis is to generate Ge-$LaBr_3$ doubly gated $LaBr_3$-TAC matrices [(E_{start},t) and (E_{stop},t)] to produce γ-γ time-difference spectra. Here, the time differences delivered by the TACs of the setup are superimposed independent of the detector-detector combination only by distinguishing between the start and stop detectors. This procedure generates two independent fast-timing-array time spectra depending on whether the decay transition of the γ_{feeder}-γ_{decay} cascade provided a stop signal (the delayed time spectrum) or a start signal (antidelayed) as described in more detail in Refs. [16–18]. According to the generalized centroid difference (GCD) method and assuming no background contributions, the measurement of the relative time shift between the centroids (first moment of a time distribution) of the delayed and the antidelayed time spectra of a γ-γ cascade provides the centroid difference and corresponds to [17]:

$$\Delta C_{FEP} = C_{delayed} - C_{anti-delayed} = PRD + 2\tau, \qquad (1)$$

where PRD is the prompt response difference, which describes the linearly combined γ-γ time-walk (zero-time vs energy) characteristics of the complete fast-timing array.

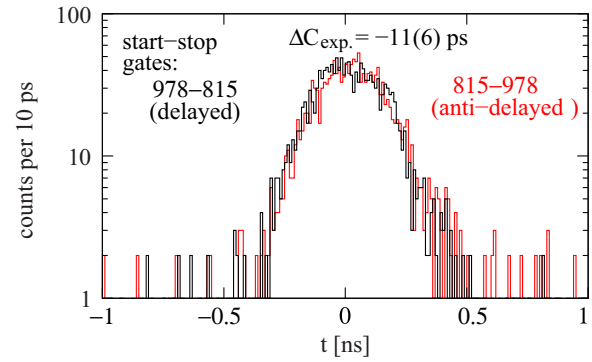

FIG. 3. Experimental time-difference spectra of the Ge(674)-gated 978–815 keV γ-γ cascade in ^{96}Sr including background contributions. The spectrum plotted in red corresponds to the antidelayed time-difference distribution.

The GCD method has several advantages, such as its mirror-symmetric representation: $\Delta C(E_{feeder},E_{decay}) = -\Delta C(E_{decay},E_{feeder})$, which translated into the $(\Delta C, E_\gamma)$ representation corresponds to:

$$\Delta C_{feeder}(E_{decay}) = -\Delta C_{decay}(E_{feeder})$$
$$\text{and} \quad PRD_{feeder}(E_{decay}) = -PRD_{decay}(E_{feeder}). \qquad (2)$$

The subscript "feeder" indicates the reference energy, thus the centroid difference is defined at the energy of the decay γ ray relative to the energy of the feeding γ ray. This transformation is done, as the shape of the PRD curve in the E_γ representation does not change. Only a parallel shift is obtained dependent on the reference energy, where the PRD curve crosses the energy axis. As a consequence, the PRD for any energy combination is derived from the $PRD(E_\gamma)$ curve using [16]:

$$PRD(E_{decay},E_{feeder}) = PRD_{feeder}(E_{decay}) - PRD_{feeder}(E_{feeder}). \qquad (3)$$

The mirror symmetry provides additional PRD data, e.g., $PRD_{feeder}(E_{feeder}) = 0$, for a precise determination of the $PRD(E_\gamma)$ curve [18]. Using a standard ^{152}Eu source and the neutron-capture reaction ^{48}Ti(n,γ)^{49}Ti, the PRD curve of the fast-timing array including the electronics setup has been determined for the energy region of 0.04–6.8 MeV [16]. The precision δPRD expressed as two standard root-mean-squared deviation (2σ) of the PRD determination is reported to be $\delta PRD = 7$ps [16].

In Fig. 3, the delayed and antidelayed time-difference spectra are presented as obtained by setting a 20-keV wide gate on the $2_1^+ \rightarrow 0_1^+$ 815-keV FEP of the projection of the Ge(674)-$LaBr_3$(978) gated $LaBr_3$-TAC matrices [see also Fig. 2(b)]. The result presented in Fig. 3 needs a time correction related to the contribution of the time-correlated Compton background, which lies underneath the two FEPs of the γ_{feeder}-γ_{decay} cascade. In order to minimize possible systematic errors, the experimental centroid difference $\Delta C_{exp.}$ is corrected using:

$$\Delta C_{FEP} = \Delta C_{exp.} + \tfrac{1}{2}(t_{cor.}(E_{feeder}) + t_{cor.}(E_{decay})), \qquad (4)$$

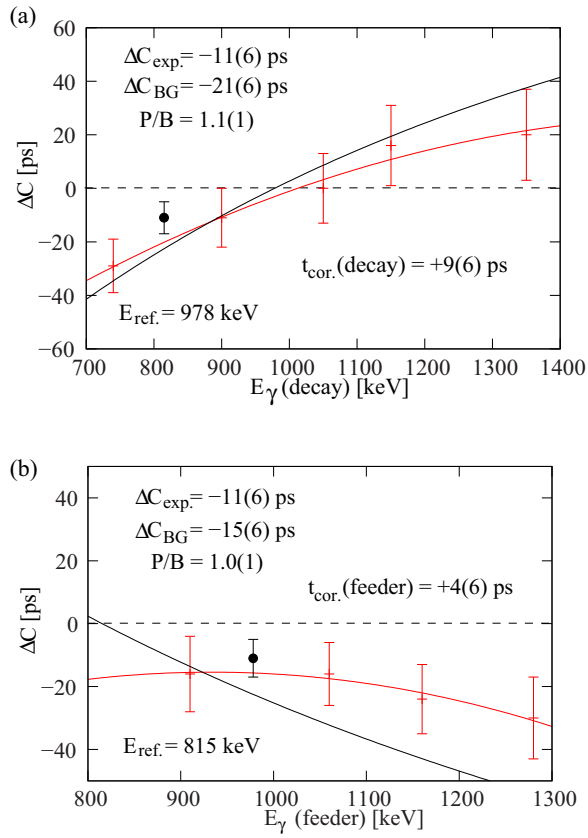

FIG. 4. (a) Determination of the background time response (online red) at 815 keV for correction using Eq. (4). The peak-to-background ratio P/B was determined from the $LaBr_3$ projection shown in Fig. 2(b). The black curve represents the PRD curve (FEP time response). The data point presented in black corresponds to $\Delta C_{exp.}$. (b) Same analysis as in (a), but for the contribution related to the background underneath the FEP of the feeding transition at 978 keV [delivered by the Ge(674)-$LaBr_3$(815) doubly gated $LaBr_3$-TAC matrices]. The final result of $\tau = 9(6)$ ps for the 2_1^+ state in ^{96}Sr is obtained using Eqs. (4) and (1) with $PRD(978,815) = -23(7)$ps.

where ΔC_{FEP} corresponds to the centroid difference related to FEP vs FEP events only. The time corrections are obtained as follows:

$$t_{cor.} = \frac{\Delta C_{exp.} - \Delta C_{BG}}{P/B}. \quad (5)$$

ΔC_{BG} is the time response of the background and P/B is the peak-to-background ratio of the considered γ ray. All these values are derived using the two Ge-$LaBr_3$ gated $LaBr_3$-TAC matrices. While P/B is obtained using the projection shown in Fig. 2(b), the background time response needs to be interpolated by generating time spectra using gates set in the background at different energies. The latter is done for energies that are higher than the Compton edge of the considered FEP. As illustrated in Fig. 4, the background timing analyses are performed with regard on the FEPs of the feeding and the decaying transition of the γ_{feeder}-γ_{decay} cascade. Here, and for visualization, the centroid difference as defined in Eq. (1) is used for both analyses instead of Eq. (2). Therefore, the PRD curve in Fig. 4(b) is inverted in order to be consistent with Eq. (1). Also, the PRD curve is shifted in parallel to cross the energy axis at the reference energy, i.e., at 978 keV in Fig. 4(a). The final lifetime uncertainty is derived as follows:

$$\delta\tau = \tfrac{1}{2}\sqrt{(\delta\Delta C_{exp.})^2 + (\delta t_{cor.})^2 + \delta PRD^2}, \quad (6)$$

whereby, $\delta t_{cor.}$ corresponds to the mean error of the two time corrections. The contribution related to the P/B uncertainty is negligible. The final lifetime result and the related uncertainty given in Table I correspond to the mean values of the results obtained using different reference energies. Similar analyses were made for lifetime determination of the 4_1^+ and (6_1^+) states in ^{96}Sr. Only an upper limit could be derived for the (6_1^+) state.

TABLE I. Mean lifetimes in even-even Sr isotopes determined from prompt-fission data of the EXILL&FATIMA experiment on ^{235}U. The corresponding fission yields are taken from Ref. [13]. The lifetimes $\tau_{Lit.}$ given in literature were derived by β-γ fast timing after β^- decay of the according Rb parent nuclei [19,20] or by safe Coulex excitation [21].

Nucleus (yield [%])	State J^π	τ ps	$\tau_{Lit.}$ ps	Reference
^{94}Sr	2_1^+	10(5)	10(4)	[19]
(4.51)	4_1^+	9(6)	$\leqslant$ 6.1	[19]
	6_1^+	$\leqslant$ 10	–	–
	3_1^-	$\leqslant$ 9	$\leqslant$ 7.1	[19]
^{96}Sr	2_1^+	9(6)	7(4)	[19]
(3.57)			5(1)	[21]
	4_1^+	10(7)	–	–
	(6_1^+)	$\leqslant$ 12	–	–
^{98}Sr	2_1^+	4.0(2) ns	4.01(12) ns	[20]
(0.81)			4.03(11) ns	[21]
	4_1^+	121(11)	115(9)	[20]
			115(7)	[21]
	6_1^+	16(9)	12(1)	[21]

Lifetimes of low-excited states in ^{94}Sr and ^{98}Sr could also be determined and are given in Table I. Due to a higher production yield, the related larger peak-to-background ratio and the ability of selecting several different Ge gates (e.g., set on the 377-keV and 458-keV transitions in the complementary fission partner ^{140}Xe), the results for ^{94}Sr given in Table I are the most precise. One example for the lifetime determination of the 2_1^+ state in ^{94}Sr is shown in Fig. 5. This example demonstrates the need for investigation of the time response of the two background components as, in general, the two components have different time responses, which can lead to time corrections with different values and even with opposite signs in certain cases.

The lifetime determination of the first 2^+ state in ^{98}Sr is illustrated in Fig. 6. Here, the 289–144 keV γ-γ cascade provides a two-component time-difference spectrum. As can be seen in the $LaBr_3$ projection of Fig. 6(a), the background events are about three times larger than the FEP events at 144 keV. From this, one can deduce that the large fast component is due

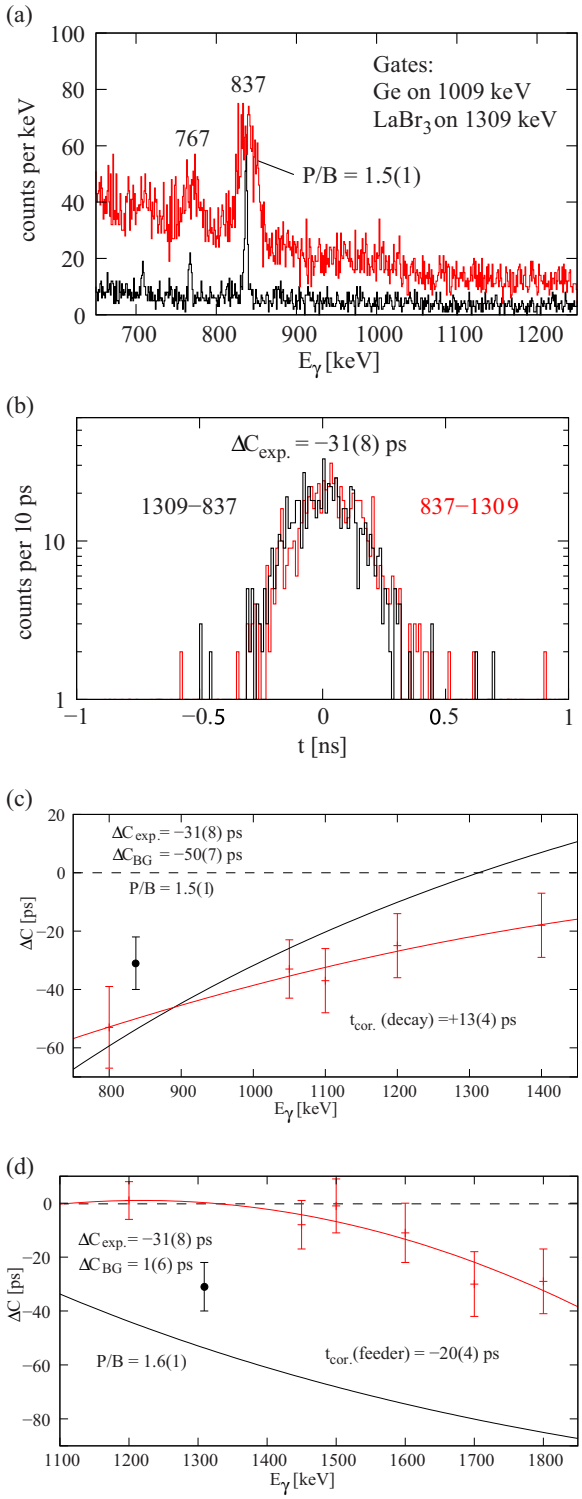

FIG. 5. (a) Doubly gated coincidence spectra showing the 837-keV $2_1^+ \rightarrow 0_1^+$ transition in ^{94}Sr. (b) Experimental time-difference spectra of the 1309–837 keV γ-γ cascade. (c) and (d) Background timing analyses for lifetime determination of the 2_1^+ state in ^{94}Sr using Eqs. (1), (4), (5). With $PRD(1309,837) = -53(7)$ps, it follows: $\tau = 9(5)$ps.

to the detection of background events. This is also confirmed by the 289–180 keV background time-difference spectrum

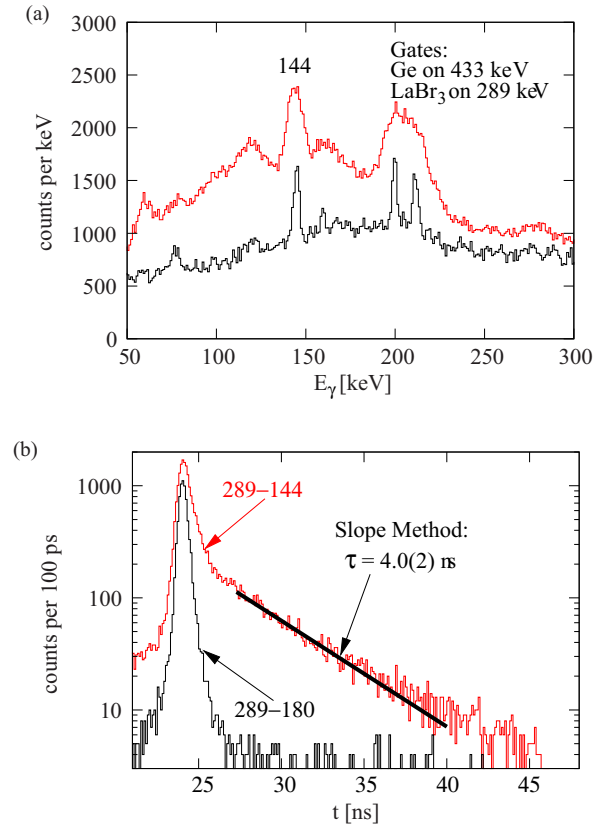

FIG. 6. (a) Doubly gated coincidence spectra showing the 144-keV $2_1^+ \rightarrow 0_1^+$ transition in ^{98}Sr. (b) Experimental time-difference spectrum of the 289–144 keV γ-γ cascade (sum of the delayed and the inverted and aligned antidelayed time spectra). The background time spectrum (black) was generated by setting a gate in the background at 180 keV [see (a)] and is shown for comparison. The slow component results from FEP detection and represents the decay of the first 2^+ state.

presented in Fig. 6(b). In such cases, the slow component can be used to obtain the lifetime directly by fitting the slope of the decay using an exponential function (slope method). Only, the uniformly distributed random background needs to be determined and fixed as a constant prior to the fit. The error here corresponds to the 2σ deviation, where 1σ is taking into account for a possible systematic error related to the choice of the fit region and the level of the random background.

In Table I, our HPGe-gated γ-γ fast-timing lifetime results are compared with values derived using different experimental techniques. All these results are consistent within the experimental uncertainties.

III. DISCUSSION

Using the measured lifetimes, the yrast $B(E2)$ values are given in Table II together with predictions of four quite different theoretical models. The Monte Carlo shell-model (MCSM) calculations were done for the description of the three Sr isotopes using the interactions given in Ref. [3] and taking into account model spaces made out of eight proton and eight neutron configurations. Beyond mean-field

TABLE II. Experimental and theoretical $B(E2)$ values of yrast states in Sr isotopes around $N = 60$.

Nucleus	State J^π	$B(E2; J^\pi \to J^\pi - 2)$ $[e^2b^2]$	$B(E2)_{\mathrm{MCSM}}$ $[e^2b^2]$	$B(E2)_{\mathrm{IBMCM}}$ $[e^2b^2]$	$B(E2)_{\mathrm{D1S}}$ $[e^2b^2]$	$B(E2)_{\mathrm{SLy4}}$ $[e^2b^2]$
^{94}Sr	$2_1{}^+$	0.020^{+20}_{-7}	0.030	0.044	0.061	0.054
	$4_1{}^+$	0.003^{+5}_{-1}	0.040	0.056	0.118	0.092
	$6_1{}^+$	> 0.008	0.004	0.048	–	0.132
^{96}Sr	$2_1{}^+$	0.025^{+51}_{-10}	0.107	0.062	0.087	0.072
	$4_1{}^+$	0.009^{+21}_{-4}	0.001	0.082	0.178	0.116
	$(6_1{}^+)$	> 0.049	0.341	0.101	–	0.332
^{98}Sr	$2_1{}^+$	0.261^{+15}_{-13}	0.250	0.196	0.146	0.274
	$4_1{}^+$	0.329^{+32}_{-27}	0.356	0.325	0.299	0.404
	$6_1{}^+$	0.335^{+188}_{-120}	0.390	0.411	0.404	0.453

calculations based on the density functional theory using the Gogny-D1S interaction in a five-dimensional collective Hamiltonian (D1S) were done by Delaroche *et al.* [22,23] and their results were recently compared with new experimental data in ^{96,98}Sr [21]. Similar calculations using the SLy4 force are taken from Ref. [24], where this force in contrast to the PC-PK1 force was able to reproduce the sudden onset of deformation in the Sr isotopes. Interacting boson model calculations with configuration mixing (IBMCM) using Hartree-Fock-Bogoliubov calculations based on the Gogny-D1M energy density functional were recently done for all even-even Ru, Mo, Zr, and Sr isotopes [25].

The MCSM predictions for the level schemes of the ^{94,96,98}Sr isotopes are shown in Fig. 7. Since the rapid shape transition in these isotopes is caused by type II shell evolution [3,4] leading to shape coexistence of different forms, the spherical, prolate, oblate, and triaxial characters of the states are indicated in this figure. In Table II the theoretical $B(E2)$ values are given. The effective charges used in the new MCSM calculations are $e_p = 1.3e$ and $e_n = 0.6e$, the same ones that were determined from the global fit to the Zr isotopes [3]. The overall trend in the data is well reproduced. Especially, the rapid change of the ground-state property at $N = 60$, interpreted as an oblate to prolate quantum phase transition, and the strong prolate deformation in ^{98}Sr are very well described by the MCSM. Remarkably, the very small $B(E2; 4^+ \to 2^+)$ in ^{96}Sr is calculated as forbidden transition between prolate and oblate states. However, the similarly very small $B(E2; 4^+ \to 2^+)$ in ^{94}Sr is overestimated by the MCSM. Better agreement might be obtained by further calculations taking into account experimental data of other Sr isotopes and by fine tuning the calculations.

Of the three models based on density functional theory, the one using the SLy4 force is closest to the data. Similarly to the MCSM predictions, it is able to describe qualitatively the sudden onset of deformation in ^{98}Sr, although the $B(E2)$ values of this isotope seem slightly overestimated. This model also gives a picture of an oblate to prolate shape transition from ^{96}Sr to ^{98}Sr. For the other two calculations (IBMCM and D1S) a more gradual phase transition results with largely underestimated $B(E2; 2^+ \to 0^+)$ value in ^{98}Sr.

IV. CONCLUSION

Seven lifetimes and three lifetime limits were measured for the yrast states in the ^{94,96,98}Sr isotopes using the EXILL&FATIMA γ-ray spectrometer to perform fast electronic timing on fission products produced after cold-neutron capture in ^{235}U. For the known cases given in literature, the results are consistent within the experimental uncertainties. A new lifetime result for the $4_1{}^+$ state in ^{96}Sr and new upper limits for the $6_1{}^+$ state in ^{94}Sr and ^{96}Sr could be determined. The deduced $B(E2)$ values are compared to state-of-the-art Monte Carlo shell-model calculations and confirm that the quantum

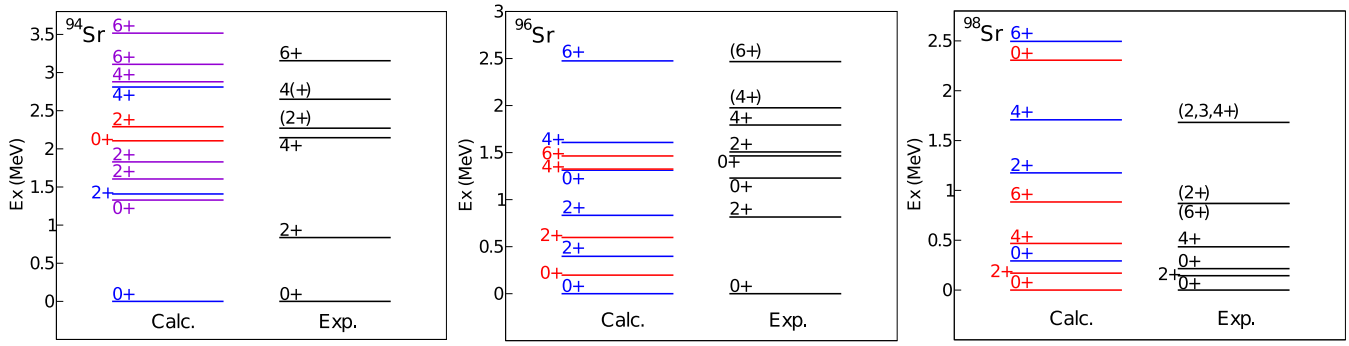

FIG. 7. Comparison between level schemes from MCSM calculations and experimental values for the lowest two excited $I^\pi = 0^+, 2^+, 4^+, 6^+$ states in ^{94,96,98}Sr. Oblate (prolate) deformed states are given in blue (red) and triaxial ones in purple. The experimental data are taken from Refs. [21,26].

phase transition occurs also in Sr isotopes similarly to the Zr isotopes at $N = 60$, as a consequence of the type II shell evolution involving many proton particle-hole excitations to the $g_{9/2}$ orbit from the pf shell. A comparison with three published energy density functional based calculations yields the best agreement when using the SLy4 force. The two models indicate for an oblate to prolate shape transition from ^{96}Sr to ^{98}Sr.

ACKNOWLEDGMENTS

We would like to thank J. M. Yao and K. Nomura for making available results of their calculations not shown in Refs. [24,25]. This work was supported by NuPNET and the German BMBF by Contracts 05P12PKNUF and 05P12DRNUP, the Spanish MINECO via Projects FPA2010-17142, CPAN (CSD 2007-00042) and PRI-PIMNUP-2011-1338 within the ERA-NET NuPNET call for translational joint activities, the UK STFC Contract No. DNC7RP01/4 and the UK National Measurement Office. The EXILL&FATIMA campaign would not have been possible without the support of several services at the ILL and the LPSC. We are grateful to the EXOGAM Collaboration for the loan of the detectors, to GANIL for assistance during installation and dismantling, and to the FATIMA Collaboration for the provision of $LaBr_3$(Ce) detectors and analog electronics. Theoretical studies including MCSM calculations were supported in part by JSPS Grants-in-Aid for Scientific Research (23244049), in part by HPCI Strategic Program (hp150224), in part by MEXT and JICFuS and Priority Issue on Post-K computer (Elucidation of the fundamental laws and evolution of the universe) (hp160211), and by the CNS-RIKEN joint project for large-scale nuclear structure calculations.

[1] P. Federmann and S. Pittel, Phys. Lett. B **69**, 385 (1977).
[2] W. Urban *et al.*, Eur. Phys. J. A **22**, 241 (2004).
[3] T. Togashi, Y. Tsunoda, T. Otsuka, and N. Shimizu, Phys. Rev. Lett. **117**, 172502 (2016).
[4] T. Otsuka, J. Phys. G: Nucl. Part. Phys. **43**, 024009 (2016).
[5] Y. Tsunoda, T. Otsuka, N. Shimizu, M. Honma, and Y. Utsuno, Phys. Rev. C **89**, 031301 (2014).
[6] J. Jolie *et al.*, Nucl. Phys. A **934**, 1 (2014).
[7] J.-M. Régis *et al.*, Phys. Rev. C **90**, 067301 (2014).
[8] G. Bocchi *et al.*, Phys. Lett. B **760**, 273 (2016).
[9] S. Ilieva *et al.*, Phys. Rev. C **94**, 034302 (2016).
[10] L. W. Iskra *et al.*, Europhys. Lett. **117**, 12001 (2017).
[11] P. Spagnoletti *et al.*, Phys. Rev. C **95**, 021302 (2017).
[12] *Extended Density Functionals in Nuclear Structure Physics*, edited by G. A. Lalazissis, P. Ring and D. Vretenar, Lecture Notes in Physics 641 (Springer, Heidelberg, 2004).
[13] T. R. England and B. F. Rider, Report No. LA-UR-94-3106, ENDF-349, 1994, https://t2.lanl.gov/nis/publications/endf349.pdf.
[14] H. Abele *et al.*, Nucl. Instrum. Methods Phys. Res., Sect. A **562**, 407 (2006).
[15] W. Urban *et al.*, JINST **8**, P03014 (2013).
[16] J.-M. Régis *et al.*, Nucl. Instrum. Methods Phys. Res., Sect. A **763**, 210 (2014).
[17] J.-M. Régis *et al.*, Nucl. Instrum. Methods Phys. Res., Sect. A **726**, 191 (2013).
[18] J.-M. Régis *et al.*, Nucl. Instrum. Methods Phys. Res., Sect. A **823**, 72 (2016).
[19] H. Mach *et al.*, Nucl. Phys. A **523**, 197 (1991).
[20] H. Mach *et al.*, Phys. Lett. B **230**, 21 (1989).
[21] E. Clément *et al.*, Phys. Rev. Lett. **116**, 022701 (2016).
[22] J.-P. Delaroche, M. Girod, J. Libert, H. Goutte, S. Hilaire, S. Péru, N. Pillet, and G. F. Bertsch, Phys. Rev. C **81**, 014303 (2010).
[23] http://www-phynu.cea.fr/science_ligne/carte_potentiels_microscopiques/tables/HFB-5DCH-table_eng.html.
[24] H. Mei, J. Xiang, J. M. Yao, Z. P. Li, and J. Meng, Phys. Rev. C **85**, 034321 (2012).
[25] K. Nomura, R. Rodriguez-Guzmán, and L. M. Robledo, Phys. Rev. C **94**, 044314 (2016).
[26] National Nuclear Data Center, www.nndc.bnl.gov.